CZECH TECHNICAL UNIVERSITY in Prague

Faculty of Mechanical Engineering - Department of Mechanics, Biomechanics and Mechatronics

BACHELOR'S THESIS

A computation of residual stress in a surface layer due to the use of Laser shock peening technology

Vojtěch Petiška **2022**

ZADÁNÍ BAKALÁŘSKÉ PRÁCE

I. OSOBNÍ A STUDIJNÍ ÚDAJE

Příjmení: **Petiška** Jméno: **Vojtěch** Osobní číslo: **491172**

Fakulta/ústav: **Fakulta strojní**

Zadávající katedra/ústav: **Ústav mechaniky, biomechaniky a mechatroniky**

Studijní program: **Teoretický základ strojního inženýrství**

Studijní obor: **bez oboru**

II. ÚDAJE K BAKALÁŘSKÉ PRÁCI

Název bakalářské práce:

Výpočet zbytkového napětí v povrchové vrstvě při použití technologie Laser shock peening

Název bakalářské práce anglicky:

A computation of residual stress in a surface layer due to the use of Laser shock peening technology

Pokyny pro vypracování:

Proveďte rešerši technologie Laser shock peening (LSP) a souvisejících problematik.
Vytvořte metodologii výpočtu Metodou konečných prvků (MKP) k určení vlivu technologie LSP na poloprostor s užitím materiálového modelu ideální elasto-plasticity. V prvním kroku simulujte statické zatížení a odlehčení poloprostoru. Velikost elementu sítě určete na základě testu konvergence sítě. Následně řešte úlohu explicitním řešičem za účelem simulace šíření napěťové vlny vyvolané tlakovou okrajovou podmínkou. Popište v tomto případě způsob určení velikosti elementu MKP sítě. V obou případech komentujte vzniklá zbytková napětí.
Ve vybrané průmyslové aplikaci diskutujte přínos a výhody technologie LSP vůči jiným konvenčním metodám opracování povrchové vrstvy.
Popište limity zkoumání efektu technologie LSP jak z hlediska simulací, tak z hlediska strojírenské technologie.

Seznam doporučené literatury:

[1] W. Braisted, R. Brockman, Finite element simulation of laser shock peening. In: International Journal of Fatigue. 1999; 21; 719-724
[2] K. Ding and L. Ye. Laser Schock Peening Performance and Process Simulation. Woodhead publishing limited. 2006
[3] J. Brajer, Effect of Laser Shock Processing Technology on Surface Integrity. Czech Technical University in Prague. 2018.

Jméno a pracoviště vedoucí(ho) bakalářské práce:

Ing. Vilém Klepač odbor pružnosti a pevnosti FS

Jméno a pracoviště druhé(ho) vedoucí(ho) nebo konzultanta(ky) bakalářské práce:

Datum zadání bakalářské práce: **12.04.2022** Termín odevzdání bakalářské práce: **14.08.2022**

Platnost zadání bakalářské práce: _____

Ing. Vilém Klepač	doc. Ing. Miroslav Španiel, CSc.	doc. Ing. Miroslav Španiel, CSc.
podpis vedoucí(ho) práce	podpis vedoucí(ho) ústavu/katedry	podpis děkana(ky)

III. PŘEVZETÍ ZADÁNÍ

Student bere na vědomí, že je povinen vypracovat bakalářskou práci samostatně, bez cizí pomoci, s výjimkou poskytnutých konzultací. Seznam použité literatury, jiných pramenů a jmen konzultantů je třeba uvést v bakalářské práci.

. _____ _____

Datum převzetí zadání Podpis studenta

Anotation

Author's name:	Vojtěch Petiška
Thesis title:	A computation of residual stress in a surface layer due to the use of Laser shock peening technology
Czech title:	Výpočet zbytkového napětí v povrchové vrstvě při použití technologie Laser shock peening
Academic year:	2021/2022
Department:	12105 - Department of Mechanics, Biomechanics and Mechatronics
Study program:	Theoretical basis of mechanical engineering
Contracting authority:	Institute of Thermomechanics of the Czech Academy of Sciences
Supervisor:	Ing. Vilém Klepač
Bibliographic data:	Number of pages: 39 Number of figures: 21 Number of equation: 31
Keywords:	Plasticity, Laser shock peening, FEM, residual stress
Klíčová slova:	Plasticita, Laser shock peening, MKP, zbytkové napětí

Abstract:
This thesis deals with numerical simulations of Laser shock peening technology using the finite element method. Based on the computational model for static and dynamic load, the values of residual stress in the surface layer after the use of this technology is determined. The computational methodology was created on axisymmetric model using the perfect elastic-plastic material model.

Abstrakt:
Tato práce se zabývá numerickou simulací technologie Laser shock peening Metodou konečných prvků. Na základě výpočtového modelu při statickém i dynamickém zatěžování jsou určeny hodnoty zbytkového napětí v povrchové vrstvě po použití této technologie. Byla vytvořena metodologie výpočtu na osově symetrickém modelu při použití ideálně elasto-plastického materiálu.

I hereby declare that this thesis is my own work. Where other sources of information have been used, they have been acknowledged and referenced in the list of used literature and other sources.

Date: . . . .

Signature

Acknowledgements

I would like to express my heartfelt thanks to my supervisor Ing. Vilém Klepač for his patience, support and guidance. Next, I would like to thanks to my family for their support during my studies, without witch I would not have succeeded.

Vojtěch Petiška

Contents

List of abbreviations and symbols **5**

List of Figures **6**

1 Introduction **9**

2 Research **11**

2.1 Tool wear . . . 11
2.2 Fatigue . . . 12
2.3 Isotropic plasticity . . . 15
2.3.1 Static plasticity . . . 17
2.3.2 Strain-rate dependent plasticity . . . 17
2.4 Laser shock peening . . . 19
2.4.1 History of LSP . . . 19
2.4.2 Technology . . . 19
2.4.3 Purpose of LSP and the results control . . . 20
2.4.4 Comparison with other peening processes . . . 20
2.4.5 Lasers . . . 21
2.4.6 Application . . . 21

3 Numerical simulations **23**

3.1 Numerical model . . . 23
3.2 Static load . . . 24
3.2.1 Mesh size . . . 25
3.2.2 Material model . . . 27
3.3 Dynamic load . . . 28
3.3.1 Mesh size . . . 29
3.3.2 Material model . . . 31

4 Results **32**

4.1 Static load . . . 32
4.2 Dynamic load . . . 33

5 Conclusions **39**

References **40**

List of abbreviations and symbols

HCP	Hexagonal close-packed
FCC	Faced-centered cubic
BCC	Body-centered cubic
TSBH	Tension split Hopkinson pressure bar
LSP	Laser shock peening
SP	Shot peening
FEM	Finite element method

M [kg]	Mass
N [-]	Number of cycles
σ [MPa]	Stress
ε [-]	Strain
S [m^2]	Cross-section
Ψ [-]	Contraction
E [MPa]	Young's modulus
A,B,C [-]	Constants
$\dot{\varepsilon}[-]$	Rate-dependent strain
P [W]	Power
E [J]	Energy
x [m]	Length
p [MPa]	Pressure
p^{cr} [MPa]	Critical load of stress
Y [MPa]	Yield stress
τ [MPa]	Shear stress
G [MPa]	Shear modulus
ν [-]	Poisson's ratio
t [s]	Time
λ [m]	Wavelength
u [$\mathrm{m} \cdot \mathrm{s}^{-1}$]	Speed
$\rho[\mathrm{kg} \cdot \mathrm{m}^{-3}]$	Density
C [-]	Courant number
κ [-]	Shakedown coefficient

List of Figures

1 LSP physical background [14]. 9
2 Tool wear. 11
3 S-N curve [16]. 12
4 Manson-Coffin curve [16]. 12
5 Paris curve [16]. 14
6 Stress-Strain curves with hardening models. 15
7 Taylor impact test. 18
8 SHPB. 18
9 LSP [6]. 19
10 Surface before and after use of LSP [13]. 22
11 boundary condition for axisymmetric specimen 23
12 Course of stress in time domain. 24
13 Mesh convergence test 25
14 Material model for static load. 28
15 Amplitude course of stress. 29
16 Static load 32
17 Dynamic load 34
18 Shear pressure. 35
19 Residual stress. 35
20 Course of the residual stresses. 36
21 Comparison of pulses. 37

1 Introduction

In mechanical engineering, it is common to harden materials and tools in order to improve its properties. For many reasons, special attention is paid on the surface layer. On many applications, the surface layer is treated by a pressure causing plasticization of material that leads to the occurrence of residual stresses after the pressure relief. The magnitude of the residual stresses determines the hardening effect.

Residual stresses prevents material against nucleation of microcracks. If the tool is treated well, it arises resistance against fatigue during high-cycle processes.

Conventional hardening processes is insufficient for complex geometries. Moreover, these technologies have poor repeatability and control of set-up. The main topic of this thesis is modeling of Laser schock peening (LSP) process, that provides possibility of material treatment with precise set-up of parameters and targeting on geometry. Principle of LSP is shown in Figure 1. The laser pulse instantly evaporate water layer on the surface and it generates a pressure wave that affects the material.

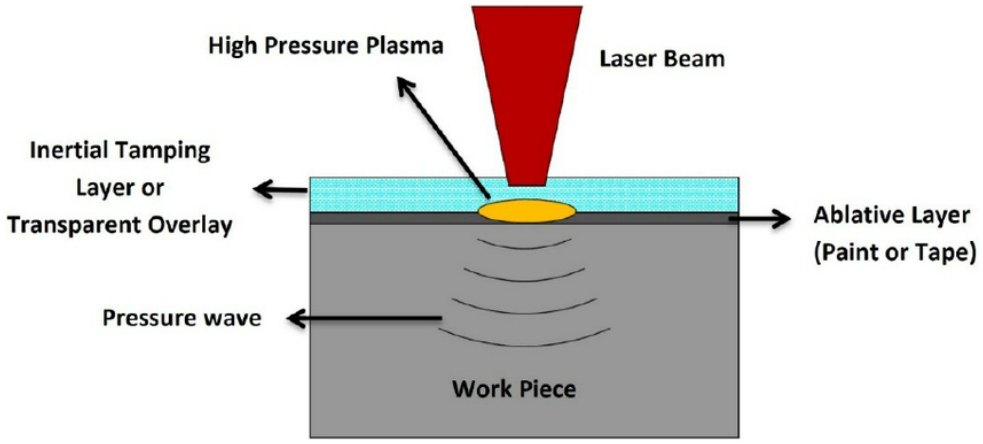

Figure 1: LSP physical background [14].

In the present thesis, the methodology for finite element method (FEM) simulation was done. The methodology can help with computation of residual stresses in a surface layer due to the use of LSP technology. Moreover, simulations help to understand the LSP process in general. The simulation was done on simplified axisymmetric model in commercial FEM software Abaqus.

Goals of the thesis are simulations of pressure impact on surface layer that represents the laser pulse. The computed data shows residual stresses in diagrams that demonstrates the effect of applied pressure. Different types of laser pulse used in the model are compared, accuracy of simulation and sufficiency of effect caused by applied pressure were evaluated.

The thesis is structured as follows. First, in Section 2, the theoretical knowledge is gradually described. It explains problematics of tool wear, material fatigue and isotropic plasticity and should serve to better understanding of LSP and other problematics related to the modeling of this physical problem. In Section 3 the numerical solution is described. It includes the creation of mesh, set-up of time increment and force and kinematic boundary conditions. It presents two approaches of modeling of surface treatment. Results, especially obtained zones of residual stresses, are presented and discussed in Section 4.

2 Research

This section summarizes most of the knowledge that is required in order to model the LSP process. Problematics related to this type of treatment are tool wear, fatigue, plasticity and LSP in general.

2.1 Tool wear

LSP have many fields of application, however this thesis is motivated by treating of tools for machining. In every machining process, all tools degrade by many types of wearing. This is caused by long term permanent stress in combination with high temperature that comes from friction. Stress is pointed on face and back of the tool and also the thermal load is asymmetric and cyclic. These factors have a marcant effect on a material. Vast of tool wearing processes exist.[3]

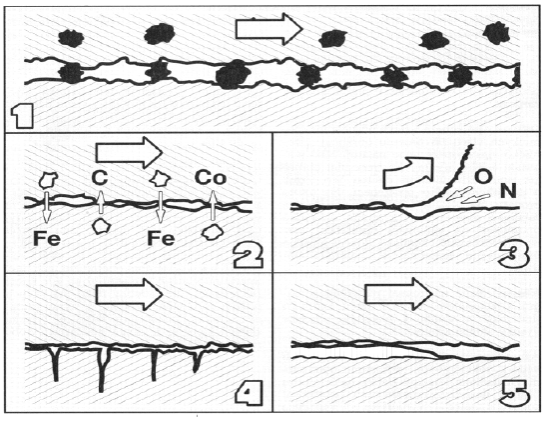

Figure 2: Tool wear.

Tool wearing processes are shown in the Figure 2. Probably the most damaging is abrasion (1) that is unwanted increased friction, caused by micro particles with same hardness as the tool that were formed during the process from the tool and the material. Adhesion (5) where two surfaces have a tendency to cling to each other, diffusion (2) of different chemical elements, or brittle crack of the surface (4). Also corrosion (3) and plastic deformation have to be mentioned, but there are many others. Combination of mechanical, chemical and thermal wears generate very complex negative affect on the tool.

The mass loss can be measured for example by weight method that consist in weighting of tool before and after work and measuring the difference:

$$\Delta M = M_1 - M_2 \tag{1}$$

where ΔM is the mass loss, M_1 is weight before wear and M_2 is weight after wear.

2.2 Fatigue

Materials exposed to regular cyclic process are affected by fatigue. Here, the term of fatigue represents degradation of material caused by cyclic loading. The level of stress during cyclic loading must be much lower than yield stress, i.e.

$$\sigma < \sigma_c^* << \sigma_y, \tag{2}$$

where σ is nominal stress, σ_c^* is reduced fatigue limit and σ_y is yield stress. The fatigue is caused by a number of repetitions of the load during which the material structure is changing. In a literature, such as [31] and [16], into following types the fatigue is distinguished: low-cycle, high-cycle and giga-cycle. The low cycle fatigue has the strongest relation with the content of this work, since the low-cycle fatigue is always connected with the cyclic plastic deformation. The example of parts exposed to the low-cycle fatigue are pressure vessel, turbine rotor, etc.

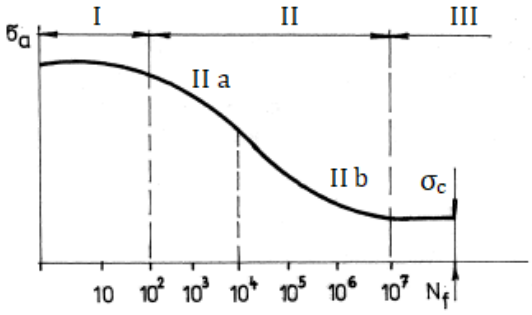

Figure 3: S-N curve [16].

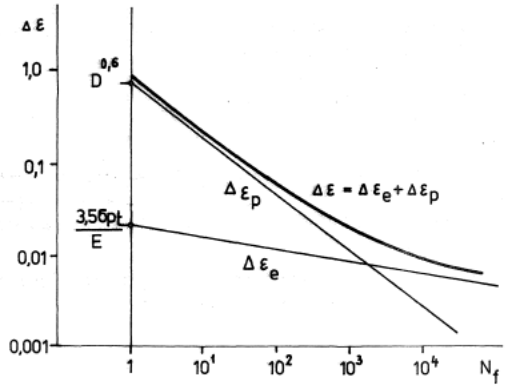

Figure 4: Manson-Coffin curve [16].

There are two plots describing behaviour of materials. S-N curve shown in Figure 3 and Manson-Coffin curve showed in Figure 4. S-N (Wohler) curve shows the number of cycles before the crack in dependency on level of loading stress [16].

There are three areas in S-N curve depending on number of cycles N_f. Static stress, finite life strength and permanent strength. Static or quasistatic strength is area under curve with less than 10^2 and it is kind of dynamic creep. Finite life strength will be divided into two parts. Low-cycle and High-cycle stress in dependency of cycles under 10^4 respectively 10^7. Over 10^7 cycles, there is a permanent stress σ_c denotes the fatigue limit [21].

The damage mechanism differs in the case of high-cycle and giga-cycle fatigue, where parts are loaded within the elastic domain of material and the damage is given due to very large number of cycles. Typically, high-cycle fatigue is factor in automotive or aerospace industry. From the other perspective, fatigue is sorted in two types: limited and unlimited lifetime fatigue. The unlimited lifetime fatigue is represented by section III in the S-N curve (Figure 3). Section I is area of quasi-static strength that is not a fatigue regime in fact. Section II is limited lifetime fatigue divided into low-cycle and high-cycle fatigue. The velocity of deformation also depends a lot on a kind of stress. Cyclic loading types are generally divided to types as follows: Static, pulsing, transient, alternately asymmetric and alternately symmetric. In alternately symmetric loading individual fibres are stressed alternately by same size of tensile stress and compressing stress. It is the most unfavorable in terms of strength.

Manson-Coffin curve (Figure 4) also shows the number of cycles before crack but in dependency on prescribed strain. Manson-Coffin curve is usually used to visualize low-cycle fatigue.

If the material is stressed in low-cycle area, the strain can be divided into elastic and plastic part.

$$\Delta\varepsilon = \Delta\varepsilon_e + \Delta\varepsilon_p \tag{3}$$

There are empirical relationships for each part according to [16]:

$$\Delta\varepsilon_e = 3.5 \cdot \frac{\sigma_{\mathrm{Pt}}}{E} \cdot N_f^{-0.12}, \tag{4}$$

where σ_{Pt} is ultimate tensile stress and E is Young's modulus,

$$\Delta\varepsilon_p = D^{0.6} \cdot N_f^{-0.6}, \tag{5}$$

where

$$D = \ln \cdot \frac{S_o}{S_f} = \ln \cdot \frac{1}{1-\Psi}, \tag{6}$$

where S_o is origin cross-section of tested bar, S_f is cross-section of tested bar after interruption and Ψ is relative constriction (contraction) [29].

Number of cycles before the crack (damage) is called Service life and it is divided into three stages. The first one is characterized by the change of mechanical properties in whole loaded

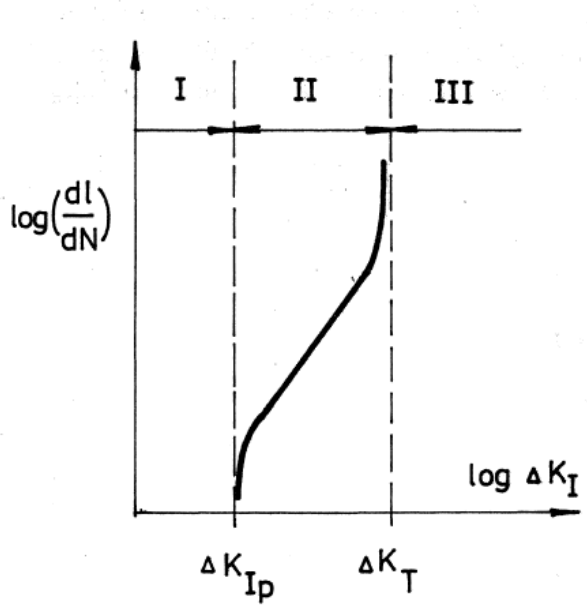

Figure 5: Paris curve [16].

material. In the second stage, the damage nucleates in smaller areas, especially on the surface an the crack is initiated.

The crack is growing and evolving into a fracture in the final stage. The length of crack nucleation and initiation can be visualised as a diagram as logarithmic function (Figure 5) [16]. But the diagram is not universal. The shape of curve depend on more variables. For example shape and size of the sample, material, surface quality, environmental impact and others [2].

For each material basal threshold exists. The basal threshold represents material resistance to crack propagation. So there is no crack propagation in material until values of tension coefficient amplitude do not reach the basal threshold. The threshold is moved after a strain relief from plastic deformation. The crack propagation would not happen in dependency on residual stresses generated in material due to plastic deformation. Dependency of crack propagation on values of tension coefficient amplitude can be also shown in diagram. But there are same variables of propagation as in nucleation of a crack.

There are materials very immune against crack nucleation, e.g. steels of 12 000 series according to [16]. In these material, the initiation of a crack last long and begin after a high number of cycles. However, when the nucleation stage is done, the crack propagation is very fast.

The whole process can be described as

$$N_f = N_i + N_c, \tag{7}$$

where N_f is total number of cycles and N_i is number of cycles until the crack initiation. For $0 < N_f < N_i$ there are no changes in the material. But for $N_f = N_i$ it can be find out the crack is initiated. Than, there is number of cycles since initiation to crack N_c.

2.3 Isotropic plasticity

Plasticity is ability of solid materials to permanent deformation. Small non-reversible changes cause hardening in structure. In isotropic plasticity it is observed experimentally that for many materials yielding is effectively independent to hydrostatic stress. This observations simplify the issue and isotropic plasticity can be applied. The strain decomposition into elastic and plastic part [28].

The beginning of initiation of plasticity is called yield stress. If the stress loaded on a material is higher than the value of yield stress, the material is being plastic deformed. The yield stress is a value experimentally measured by tensile test. The example of Stress-strain curve is shown in Figure 6.

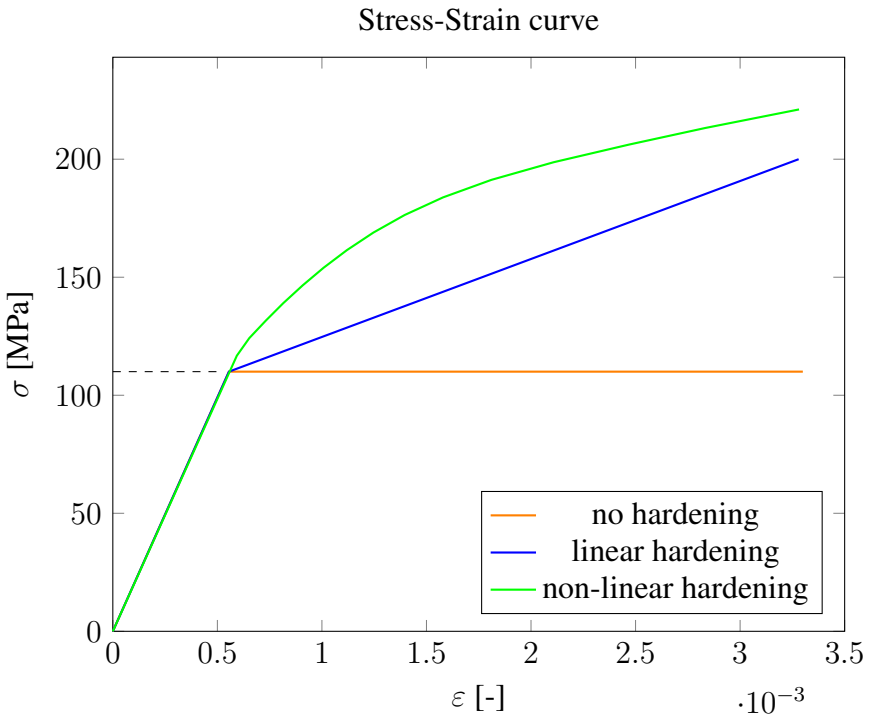

Figure 6: Stress-Strain curves with hardening models.

Than, exists elasticity that is regime of material deformation described by Hooke's law.

$$\varepsilon = \frac{\sigma}{E}, \tag{8}$$

where ε is strain, σ is loaded stress and E is Young's modulus.

When the yield point is reached, the behavior of material stops to follow Hooke's law and the material starts to employ equations of plastic flow. So the plasticity begins after stress overcome yield stress [22].

In contrast with elasticity, plasticity is irreversible. It could be understood as a regime with non-revertable changes in material. It means that after strain relief the material will not form into original state. The elastic deformation will return, but the plastic strain is permanent. Here, the assumption of small strains is adopted and total strain tensor is given as $\varepsilon^{\mathrm{tot}} = \varepsilon^{\mathrm{el}} + \varepsilon^{\mathrm{pl}}$, where $\varepsilon^{\mathrm{el}}$ is elastic strain and $\varepsilon^{\mathrm{pl}}$ is plastic strain.

The value of yield stress is represented by dashed line. On wide range of materials, the yield stress is not clearly seen from tensile curve. So the offset yield point is used to define where the material is going plastic. In a literature, such as [17] and [9] the offset yield point is defined as stress necessary to $0.2\ \%$ from relative strain. Yield stress divides dependency into elastic part that is represented by the linear line, and plastic part represented by the nonlinear curve in Figure 6 [19].

Plasticity in mechanical engineering and in my thesis will be explained on behaviour of ductile metals. Metals are usually polycrystalline aggregates which means they consist of amount of simple crystals. Crystals are three dimensional array of atoms. Most often for metals are three crystal structures. Hexagonal close-packed (HCP) (zinc and magnesium), Faced-centred cubic (FCC) (alluminium, copper, gold) and Body-centered cubic (BCC) (iron, tungsten, molybdenum) and all of them are bounded by the metallic bond. The plastic deformation is caused by crystallographic planes movement as a response to stress higher then yield stress. This problematic is described in more detail in [22], [9] and [24].

The stress overcome the metallic bonds and atoms that were bonded by them move out of their original place. The movement as a response to stress is not exclusively for atoms but is also very common for whole planes which also cause bigger deformation. Relative movement in crystal structure relates to specific planes that have the lowest resistance to slip and they move in the direction of stress. Huge number of inter-crystal slips and deformation causes a visible strain on a real specimen [1].

2.3.1 Static plasticity

The first subtopic of plasticity mentioned here is static plasticity. There is no connection to velocity of deformation is omitted. We simplify it and see the velocity as null.

It can be only use for the systems where the external loading is much slower than viscous and dynamic time scales of internal processes. Rate-independent models are suitable only if there is an interest in the slow time scales. But there are some dissipative forces, such as back stresses within cracking, plasticization or friction generated during static load. There is vast models for description of material behavior within the plasticity regime. Basic types of material hardening are shown in the Stress-Strain curves in Figure 6. These lines show in general function

$$\sigma = \sigma(\varepsilon_{\mathrm{p}}). \tag{9}$$

The orange line holds for perfectly elastic-plastic model. This model assumes no hardening and is often used for limit analysis calculations e.g. in problematic of soils [33]. After reaching the yield stress, the derivative of Equation 9 is zero. The blue line in Figure 6 represents linear hardening (bi-linear model). It is also simplified but can be applied on specific materials. Hardening line has its own slope line that is smaller than slope line of elastic line described by Hooke´s law. Non-linear hardening is represented by green curve. There are many of models describing non-linear hardening.
Examples of non-linear plasticity models:
Power law hardening:

$$\sigma = C\varepsilon^n \tag{10}$$

Johnson-Cook model:

$$\sigma = A + B\varepsilon_{pl}^n \tag{11}$$

Voce model:

$$\sigma = \sigma_y + C(1 - e^{-k\varepsilon_{pl}}) \tag{12}$$

The model application is dependent on exact material and how the material is used. The performance of models differ for each material.

2.3.2 Strain-rate dependent plasticity

Strain-rate-dependent plasticity respects affect of strain velocity. As well as in the case of static plasticity, in strain-rate-dependent plasticity, there's wide range of models that deals with capturing of material behavior in range of high strain-rates [8]. The Johnson-Cook model

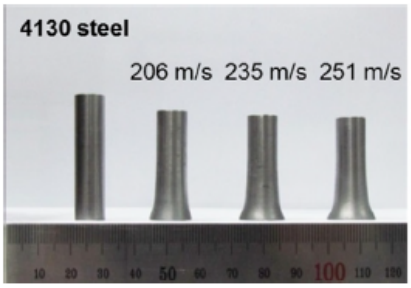

Figure 7: Taylor impact test.

Figure 8: SHPB.

consists of three independent parts. First part shows the stress value as a function of plastic strain. If there are no more parts, the model would describe rate-independent (static) plasticity. The second one shows dependence on the strain-rate [27].

$$\sigma(\varepsilon, \dot{\varepsilon}, T) = [\sigma_r(\varepsilon_p)] \cdot [\sigma_{\dot{\varepsilon}}(\dot{\varepsilon})] = [A + B\varepsilon_p^n] \cdot \left[1 + C \ln \frac{\dot{\varepsilon}}{\dot{\varepsilon}_0}\right] \tag{13}$$

To identify parameters of material model in general, experimental data must be provided. Description of determination of model parameters can be found in [32]. Thermal impact, machining simulation, finite element models and many other importants are in this list. For observing of material properties in the range of high strain-rates we mention Taylor test and Hopkinson split bar [26].

In the Figure 7 specimens after the Taylor test are shown. One can see the effect of impact velocity on the deformed shape of specimen. Specimens are made of the observed material and the material parameters can be calibrated on the deformed shape. Another observed outcome of the Taylor test is the propagation of the wave generated by the impact of the specimen on the experimental bar.

Tension split Hopkinson pressure bar (SHPB) is depicted in Figure 8. During this test, there is a sample in between two symmetrical bars. There are generated shocks into this bar that generates shock wave. The result of observation is transition of the wave through the specimen and the strain and residual stresses left after. Results of these tests are used for calibration of material model parameters [30].

The reason of using these models is to simulate work (strain) hardening. It is the process where the crystal dislocations and surface strain generates residual stresses. The reason why these negative residual stresses are required on the surface of tools is its prevention of crack initiation while healing micro-cracks in the surface and either prevention of their nucleation. It causes

better fatigue life during service of the treated part [18].

2.4 Laser shock peening

Laser shock peening (LSP) is method used in terminal machining. It provides advantages in possibility of good control of intensity of process and repetition of treating.

2.4.1 History of LSP

In 1960s, when it was invented, it improved and enriched conventional hardening techniques used at that time. More precisely, the first experiment using pulsed laser on material surface were done in USA in 1968. Scientific research till 1981 was mainly done on aluminum alloys and steel for aviation industry. The process became famous after 1983 because of patent made by American military research company. Probably the most famous and important for LSP process is General Electric company with huge research and over 23 patents concerning LSP. It became a great alternative for processes as a conventional shot peening or sanding and added new possibilities in terminal processing [6].

2.4.2 Technology

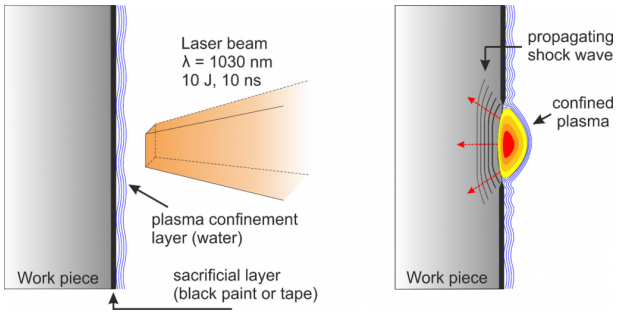

Figure 9: LSP [6].

Principle of LSP is simple and is shown in the Figure 9 [6]. The laser on the surface generates shock wave. The shock wave is going through the material and may cause plastic deformation, if the impact is strong enough. The generation of shock wave is caused by laser hitting the layer of water that is applied on the surface. The water is instantly evaporated that causes the wave generation. Some specific liquid glasses can be used instead of water as well. Size of shock wave and so the intensity of impact depends on a speed of evaporation. So there is dependency between power of laser that causes a velocity of evaporation, and intensity of deformation. To reach better quality of the surface, the protective layer is applied under the liquid. The absorbent can be protective paint, mostly used is black paint, protective tape, or aluminum foil. The real

issue is to find out all settings to generate waves that will affect material the way that is required. After the dispersion of generated waves, residual stresses remain in the material [12].

The theory of impact and transmission of waves through solids is very complicated. It depends on many factors as a type of material, temperature and others.

2.4.3 Purpose of LSP and the results control

The purpose for use of this method is improvement of properties of material in the surface layer. Next to the other properties as e.g. a better corrosion prevention, roughness, etc., residual stresses that will be computed in further sections, lead to better protection against the crack initiation and improve fatigue life. The mechanism of prevent crack invitation is described in sections 2.2 and 2.3.

The residual stresses are the most focused effect of LSP, so there is a need of measuring of it. Some methods of measuring of residual stress are as follows. Centre-hole drilling is the first one we mention. It is destructive gauge method where the result is judged just by visual control. The next one is etching method that is also destructive but can be used on harder materials, mostly on titanium specimens. Non-destructive methods are X-ray diffraction or neutron diffraction. During these measurements the specimen is not destroyed, so it can be easily used in industrial production. The X-ray provides results in a surface layer but the maximum measured depth can be over $1\ \mathrm{mm}$.

Not only residual stresses can be measured. There is also importance to measure surface hardness that is usually done by conventional methods as hardness test by Vickers, Brinnel or Rockwell [6].

2.4.4 Comparison with other peening processes

Traditional techniques of surface treatment are shot peening and sanding. The shot peening (SP) is shooting of small balls as projectiles on a surface. The balls are usually metallic or ceramic and they are shot by pneumatic accelerator by the velocity of $20 - 40\ \mathrm{m} \cdot \mathrm{s}^{-1}$. In the case of sanding, small balls are replaced by sand grains [25].

The positive aspect of LSP is also an integrity of affected area, where the exact area is known and can be regulated. The LSP can treat all the required area with the same intensity and reduces the randomness of the treatment. The SP or sanding shot the particles randomly and the surface is not hardened all over the same way.

In comparison, the magnitude of the residual stresses is comparable so no one is better in this aspect. Residual stresses extend much deeper below surface during LSP than those from SP. Thus the enhancement of fatigue life is better while using LSP. Because of principle of LSP, it is possible to treat smaller surfaces and more complex geometries than with classical SP. On the other hand, LSP is more expensive and is difficult to set, because of its complex physical background.

2.4.5 Lasers

LSP is complex issue with many variables. One of them is laser system as a source of shock wave that determines boundary conditions in simulations. Some main requisites of laser systems used to LSP are average power level in between hundreds and thousands of watts. Especially kilowatts lasers nowadays replace weaker lasers, because their higher level efficiency. Kilowatt level laser can be used instead of approx 12 basic $(25\mathrm{W} - 200\mathrm{W})$ lasers. Common laser system used in past in LSP was Neodymium-doped glass (Nd-glass) laser. Its repetition rate was too low, about one cycle every 8 minutes. It was replaced by Wagner Laser Technologies and their glass-laser system that have a repetition rate of 1 Hz, or one cycle per second. Nd-glass laser was improved now, and the system can deliver pulse energy of $25\,\mathrm{J} - 100\,\mathrm{J}$, pulse duration about $30\ \mathrm{ns}$ and power level $1\ \mathrm{kW}$ [6][12].

2.4.6 Application

LSP can be used on various materials. Such as many metallic composites, including cast irons, copper, aluminium alloys, titanium and its alloys, nickel-based super-alloys and others.

LSP can be used for processing of high-value-added parts for hi-tech performance. Other applications can be on components with complex geometry next to notches, holes and corners. These are advantages of LSP-the possibility of precise targeting on critical places that comes handy in applications for tools, tipped tools or turbine vanes. There are some examples and possible improvement of their fatigue life:
Coil springs $(1000\,\%)$, gears $(1000\,\%)$, torsion bars $(600\,\%)$, welds $(200\,\%)$ and connecting rods $(100\,\%)$.

Some great examples from industry is screw-propeller where the LSP helps with fatigue life and, which is more important for this tool, improve corrosion resistance. The processing takes about a four hours thanks to kilowatt laser. Without it, the processing would take about a couple of weeks. The biggest producer of tools hardened by LSP is Rolls Royce as a producer of aircraft engines. During the processing of rotor blades, instead of using 12 basic lasers that have to work

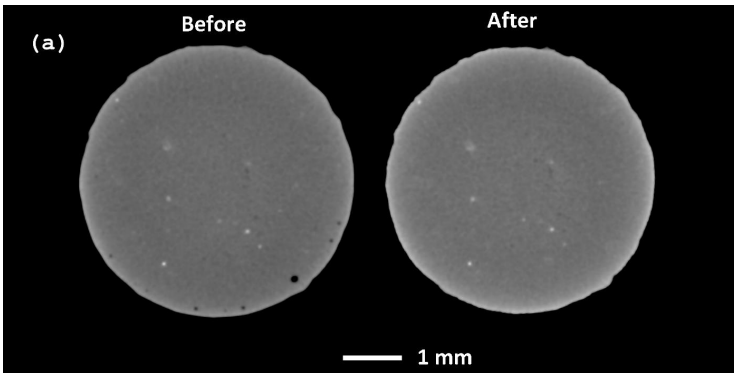

Figure 10: Surface before and after use of LSP [13].

on full power, they use one kilowatt laser so the capacity can be increased. Very interesting is also Airbus A320. It is the first mass-produced airplane using LSP process on its wings to form upper side of the wing [6].

As shown in Figure 10 that was published in [13], the surface before the treatment (left) contains small black spots that illustrates micro-scales and imperfections. The surface after the treatment (right) does not contain those black spots. This illustrative figure shows efficiency of LSP treatment.

3 Numerical simulations

The distribution of stress and the residual stress in the surface layer after the treatment were solved numerically by Finite Element Method (FEM). In engineering applications FEM is used to simulate stress distributions, deformations, heat flow, etc. on created physical model. FEM uses a an approximation of unknown variables to transform partial differential equations into algebraic equations [10]. In this thesis, for simulations of residual stresses and permanent deformation after LSP treatment, Abaqus FE software was employed. Solver "ABAQUS/Standard" is a general purpose finite element program designed specifically for advanced structural and heat transfer analysis. Also solver "ABAQUS/Explicit" will be necessary. It provides explicit transient dynamics capability [4]

3.1 Numerical model

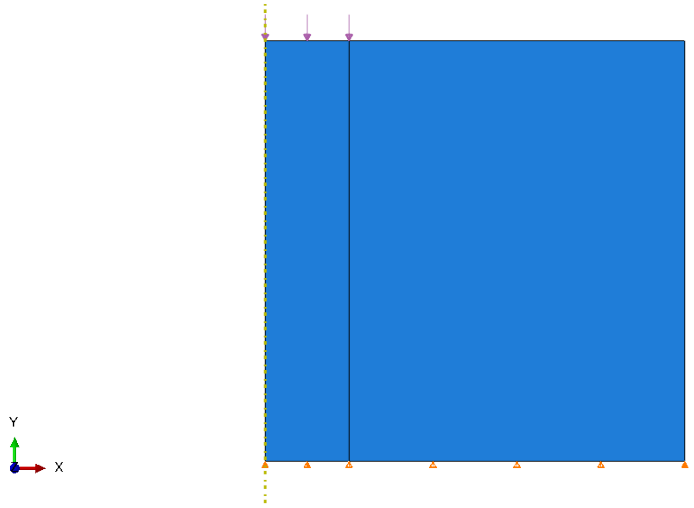

Figure 11: boundary condition for axisymmetric specimen

The specimen is cylinder with height of $100\ \mathrm{mm}$ and diameter of $200\ \mathrm{mm}$. The simulation is done on axisymmetric specimen represented by square $100\ \mathrm{mm} \times 100\ \mathrm{mm}$ shown in Figure 11. The symmetry axis is placed on the left edge, so the rest of the model rotates around it and it represents the real cylinder shape of the specimen. Zero displacement boundary condition for y direction is applied on the bottom edge.

The cylinder is split into two parts. The inner part with length of $20\ \mathrm{mm}$ is loaded with the pressure boundary condition. The amplitude of pressure boundary condition will be described in following sections separately for static and dynamic load.

3.2 Static load

The velocity of stress is null, so the momentum of material is not took into account.

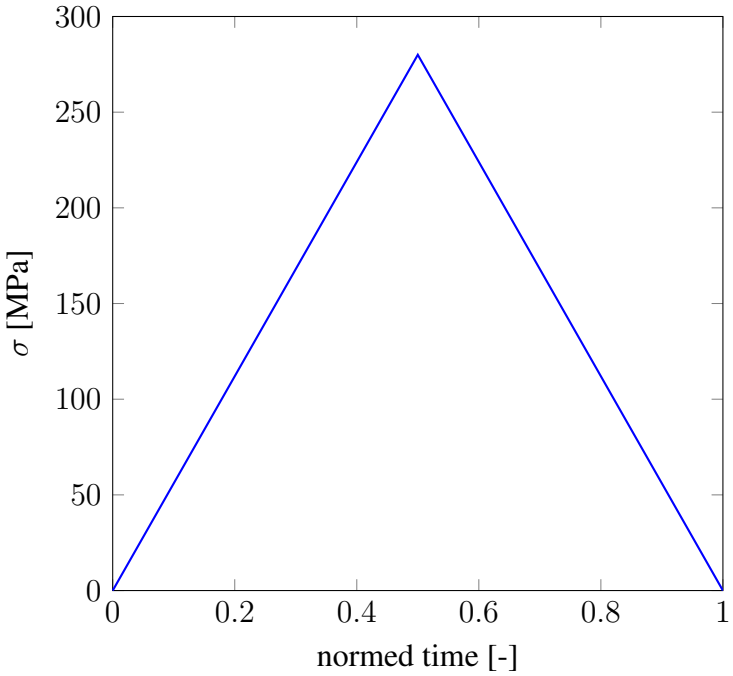

Figure 12: Course of stress in time domain.

This simulation represents loading of axisymmetric semi-space by a pressure with amplitude graphically represented by the line in Figure 12. The maximum value of pressure is 280 MPa. This value was set based on the critical load. Critical load is a maximum value of stress before plastic collapse and reads.

$$p^{\mathrm{cr}} = \frac{Y \cdot (2+\pi)}{\sqrt{3}} \tag{14}$$

$$p^{\mathrm{cr}} = \frac{100 \cdot (2+\pi)}{\sqrt{3}} = 297\ \mathrm{MPa}, \tag{15}$$

where Y is the yield stress. Computation of critical load on semi-space with perfectly elastic-plastic material is described more in detail in [15]. After substituting $Y = 100$ MPa into the equation 14, the value of critical load is $p^{\mathrm{cr}} = 297$ MPa. The equation in [15] is correct at all for plain-strain model, but this thesis uses axisymmetric model in Abaqus. So the value of critical load is not exact from this equation, but it is great to compare with second method of determination of critical load. The second method is Trial and error method using FEM software.

The value of critical load that was computed in plain-strain, was used as initial estimation.

The collapse of the structure in case of axisymmetric geometry was computed by FEM and the value of critical pressure was $p^{cr} = 280\ \mathrm{MPa}$.

In the static load solver, no time is required, so the normed time is used for setting the amplitude loading. In the first half of the time the stress is growing and the second half is for static relief.

3.2.1 Mesh size

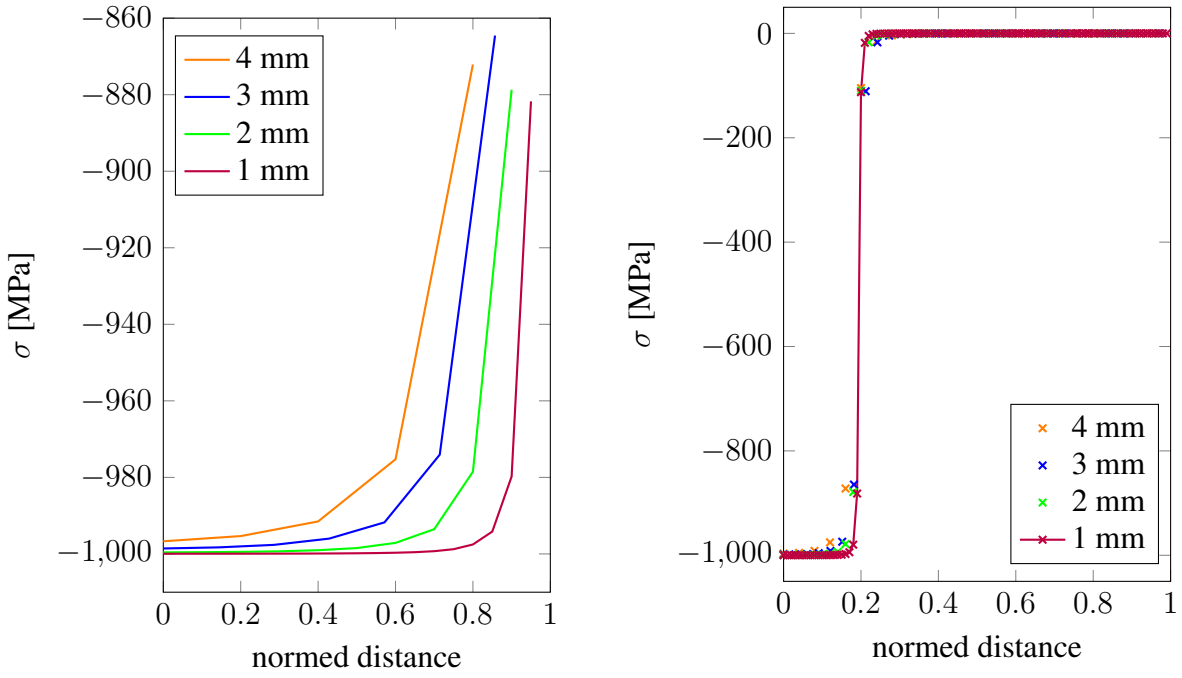

(a) Horizontal stress on loaded area.

(b) Horizontal stress on whole surface.

Figure 13: Mesh convergence test

Another necessary setting in FEM simulation is mesh. Mesh divides the specimen on individual elements. The calculations take every single element by its own. The mesh size is lower, the finer is the mesh. If the mesh is not fine enough, elements are too big and calculation is not accurate. On the other hand, if the mesh is fine a lot, total computational time is too high. For these reasons, the mesh convergence test was done.

The loaded pressure used in mesh convergence test is force boundary condition with magnitude $1\ 000\ \mathrm{MPa}$. The distribution of pressure is uniform on whole loaded area.

Mesh convergence test is observing of computed values in dependency on the mesh size. In this thesis it is done by comparing smoothness of curves in 13(a) and 13(b).

Diagrams shows dependency between pressure and normed distance.

Many types of stress can be set in Abaqus. Some of them only depend on the direction of a stress. σ_{11} represents stress in the direction of "x" axis, σ_{22} the direction of "y" axis. σ_{33} is now irrelevant, because represents the direction of "z" axis, but the model is two dimensional. σ_{12} represents shear stress.

Some of them depend on calculation. For example reduced stress by Mises or stress by Tresca. These reduced stresses by Mises and Tresca are well explained in [23] and they are also shown in Mohr's circles.

Mises hypothesis also known as "The maximum distortion criterion" or "Energetic hypothesis" [16] presumes reduced final stress as:

$$\sigma_{eq} = \sqrt{\sigma_x^2 + \sigma_y^2 - \sigma_x \cdot \sigma_y + 3 \cdot \tau_{xy}^2}, \tag{16}$$

where σ_x equals to σ_{11}, σ_y equals to σ_{22} and τ_{xy} equals to σ_{12}.

Second type of reduced stress is by Tresca also known as Maximum shear stress hypothesis presumes reduced final stress as:

$$\sigma_{eq} = max\left(\left|\sigma_1 - \sigma_2\right|; \left|\sigma_1\right|; \left|\sigma_2\right|\right), \tag{17}$$

resp.

$$\sigma_{eq} = max\left(\left|\sqrt{(\sigma_x - \sigma_y)^2 + 4\tau_{xy}}\right|; \left|\sigma_1\right|; \left|\sigma_2\right|\right), \tag{18}$$

where σ_1 and σ_2 are principal stresses. Principal stress is normal stress in a plane in which the shear stresses are equal to zero.

The dependency in Figure 13(a) and Figure 13(b) is between pressure σ_{22} (in the direction of y axis) and normed distance of pressure loaded area. In the diagram, it is seen that the most affected part is in the middle of cylinder (normed distance 0). Both diagrams shows the same dependency from the computing. The Figure 13(a) is detail of Figure 13(b) and shows loaded stress in the surface of the area with the force boundary condition on it. The second picture shows profile of loaded stress on the whole surface.

The Figure 13 proves that mesh size 1 is fine enough to be employed to computations. In the

Figure 13(b) is possible to see the deviations among results of stresses numerically calculated based just on the mesh size. The deviations are not negligible. In following simulations in static part, the mesh size 1 will be used.

3.2.2 Material model

The material model used in this thesis is perfectly elastic-plastic model. The model should represent materials that are most often used in Laser shock peening technology. The elastic area of the material model is going to be linear. For the plastic behaviour ideal elastic-plastic model was chosen. It is model with no hardening.

In this work, materials are set by mechanical constants. Young´s modulus and Poisson´s ratio are set in order to describe elastic behaviour. For description of plastic behaviour, stress-strain dependency was set as a constant.

According to [34], Young´s modulus (E) is material property measured by tensile test that gives the dependency between stress (σ) and strain (ε).

$$E = \frac{\sigma}{\varepsilon} \tag{19}$$

In elastic area, Young´s modulus is capt constant. Poisson´s ratio (ν) is material ratio of deformation in the direction perpendicular to the direction of loaded stress and deformation in the loaded stress direction. It is also countable from two other material constants. Young´s modulus of elasticity (E) and Shear modulus (G) in the direction of stress.

$$\nu = \frac{E}{2G} - 1. \tag{20}$$

Model, used in this thesis, is set to represent behaviour of an average steel. For that reason, Young´s modulus for this model is $E = 200\,000\ \mathrm{MPa}$ and Poisson´s ratio is $\nu = 0.3$. For this numerical study, the yield stress was estimated as $Y = 100\ \mathrm{MPa}$. Since the plasticity is ideal, the derivative of 9 is zero.

In the Figure 14 is shown Stress-strain curve of material model that was set to simulate static load.

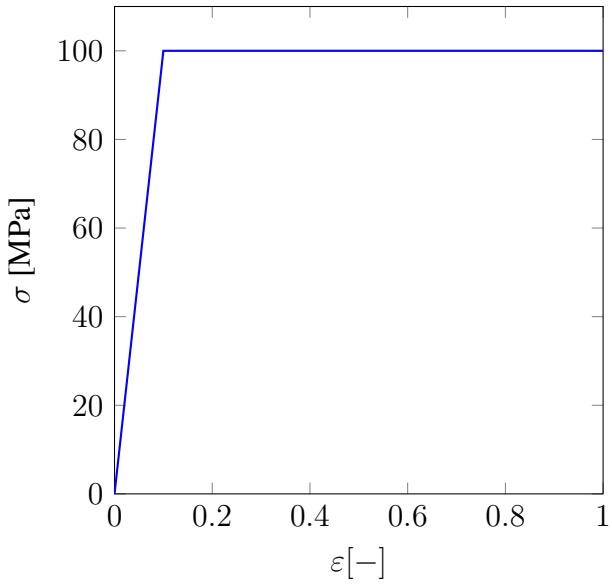

Figure 14: Material model for static load.

3.3 Dynamic load

The axisymmetric specimen for dynamic simulation is ten times smaller than for static simulation. The cylinder represented by axisymmetric half-space is $10\ \mathrm{mm}$ high with diameter of $20\ \mathrm{mm}$. The calculation time for origin specimen would be enormous but the results would be equal, so dimensions of the specimen were reduced.

For dynamic load, the Abaqus settings were changed in order to involve the momentum of material. Hence, the ABAQUS/Explicit solver was employed.

Due to its dynamic action, parameters of the shape of pulse, period and amplitude and its time distribution, have to be settled. From the experience, likewise in [11], it is known that the duration of the pulse in technology of LSP is roughly in range from $10\ \mathrm{ns}$ to $50\ \mathrm{ns}$. Different time periods represents different force. The results differs in residual stresses and the depth of plasticized area. In this work, as an example, the time period of pulse was settled as $t = 30\ \mathrm{ns}$.

In the Figure 15, the pulse course that could represent laser impact is shown by green points. The course used in simulations that illustrates approximation of the physical process of laser and surface interaction is shown in Figure 15 by the blue line. The second pulse course that is illustrated with the red line was used for demonstration of the pulse shape effect.

The laser impact was modeled as a pressure boundary condition on the top surface of the geometry. The magnitude of pressure was $2000\mathrm{MPa}$. The load distribution in time is depicted in Figure 15. The representative shape of pulse is represented by the blue line that shows classical

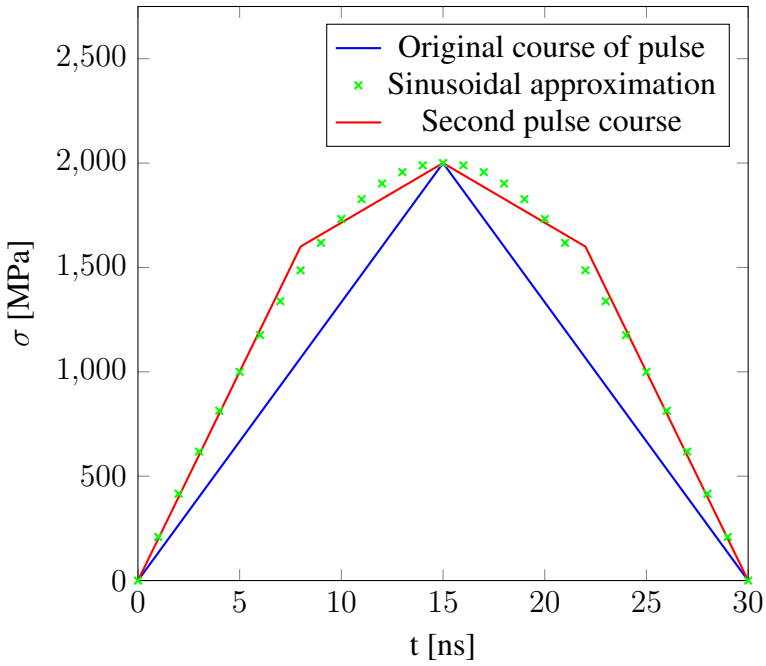

Figure 15: Amplitude course of stress.

tent function. The period is 30 ns and the shape is symmetric.

The required outcome of simulations is the residual stress that remains after the material relaxation. To run the simulation for the relaxation time would be unnecessarily computationally consuming. Hence, the time period of explicit simulation was settled to $1\ 000$ ns. This time is long enough to let the wave system evolve in agreement with the physical process and mainly with the evolution of residual stresses. To filter elastic waves, the subsequent static step was included. This procedure provides pure information about computed residual stresses and simulates the entire single laser pulse. Application of another pulses could be modeled by the repetition of presented procedure.

3.3.1 Mesh size

The main parameter for estimation of the element size is the wavelength

$$\lambda = t \cdot u, \tag{21}$$

where t is period of the highest eigenfrequency of the impact and u is the speed of elastic wave in given material. The speed of elastic wave is dependent on a material and reads

$$u = \sqrt{\frac{E}{\rho}}, \tag{22}$$

where E is Young's modulus and ρ is the density of material. The values were settled as it is typical for steel, $E = 2 \times 10^5$ MPa and $\rho = 7\,890\ \mathrm{kg} \cdot \mathrm{m}^{-3}$. According to [7], the speed of elastic wave in steel is from Equation 22

$$u = \sqrt{\frac{200 \times 10^9}{7\,890}} = 5.035 \times 10^3\ \mathrm{m} \cdot \mathrm{s}^{-1}. \tag{23}$$

For the purpose of consistency, the Young's modulus was converted to Pascals. Speed of elastic wave $u = 5.035 \times 10^3\ \mathrm{m} \cdot \mathrm{s}^{-1}$ is put into Equation 21

$$\lambda = [30 \times 10^{-9}] \cdot [5.035 \times 10^3] = 1.5 \times 10^{-4}\ \mathrm{m} = 0.15\ \mathrm{mm}. \tag{24}$$

The wavelength from Equation 24 is $\lambda = 0.15$ mm.

Based on the wavelength, the element size can be estimated. From the experience, it comes sufficient to describe the wave by at least ten spatial increments, however, more robust is general relation

$$\Delta x = \frac{\lambda}{10 \sim 20}. \tag{25}$$

For the low number of spatial increments, results would be devalued by the loss of information about the impact. On the other hand, fining of element size would generate very large mesh even on such basic geometry computed in this work. Computation on this mesh would require too much memory and could lead to the buffer overflow. Hence, after set of numerical experiments, the nominator in Equation 25 was estimated on 15. The size of spatial step is then

$$\Delta x = \frac{0.15}{15} = 11,25 \times 10^{-3}\ \mathrm{mm}. \tag{26}$$

The most general approach for estimation of the time increment uses the knowledge of the highest eigenfrequency of the mesh. In this work, non-dimensional Courant's number computed as

$$C = \frac{u \cdot \Delta t}{\Delta x} \tag{27}$$

was employed. From the experience, in the case of axisymmetric geometry, the dispersion of solution on the axis is the lowest for $C = 0.5$. So it was determined here. The value of time increment is

$$\Delta t = \frac{C \cdot \Delta x}{u}. \tag{28}$$

From the equation is necessary to express the time increment in Equation 28

$$\Delta t = \frac{0.5 \cdot 11.25 \times 10^{-3}}{5.035 \times 10^{6}} = 11.25 \times 10^{-10}\ \mathrm{s}. \tag{29}$$

As it was mentioned before, the whole simulation is set for $1\ 000$ ns. The time increment calculated and set is $11,25 \times 10^{-10}$ s. It means that the computational software counts system of equations in 889 time steps during this simulation.

3.3.2 Material model

The material for dynamic load simulation has to be modified a little. Some main properties stays the same. Young's modulus is still $E = 200\ 000$ MPa and Poisson's ratio is $\nu = 0.3$. The difference starts with ideal elastic-plastic model. The yield stress, the area where the plastic behaviour starts, is 800 MPa. The chosen steel is high-strength steel according to [20] that is why the yield stress is relatively high.

In order to model propagation of waves in the structure, it is necessary to involve the momentum of material points. To do so, the density of material was added into the set of material parameters. The density was already used in Equation 22. But for consistency with other quantities that returns stress in MPa, it needs to be converted to the unit system of $T \cdot mm^{-3}$. The number value of density is then $\rho = 7.89 \times 10^{-9}\ \mathrm{T \cdot mm^{-3}}$. In general, density and other material properties changes according to temperature. However, LSP process is assumed to be isothermic, so the temperature dependency don't need to be taken into account.

4 Results

This section is devoted to description of individual results of static and dynamic load and presentation of the results of the whole simulation process. The section is divided into two parts. In the first one, the results of static load simulation is described. In the second one, the dynamic load simulation is presented and commented. Shapes of zones of residual stress in the surface layer are described in both parts for each simulation.

4.1 Static load

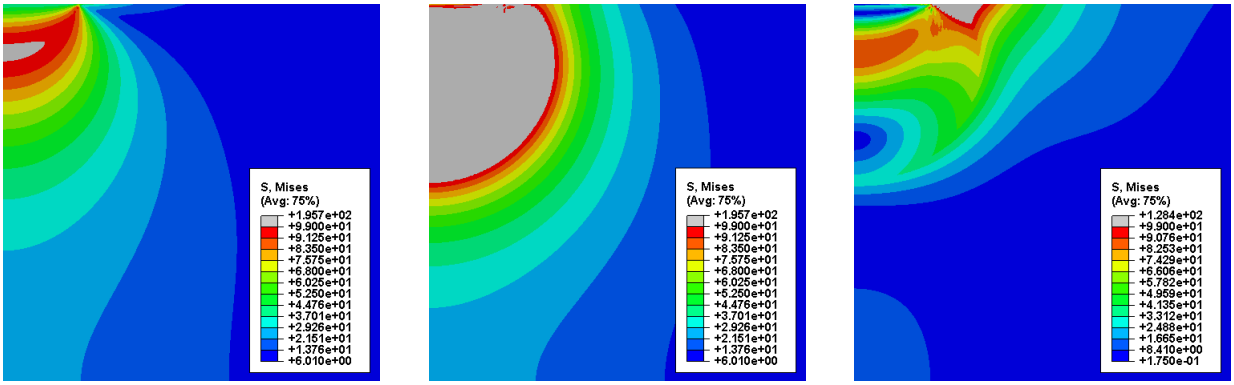

(a) Initial plastic area (b) stress after loading (c) stress after strain relief

Figure 16: Static load

The first part of this thesis was simulation of static load and relief on axisymmetric semi-space. The results of simulation are Figure 16(b) and Figure 16(c). Firstly, the output of the simulation in Abaqus are these to figures. It represents the best visualisation of stress and deformation. The colours in the figures represents pressure by Mises that was explained in 3.2.1 and it represents combination of stresses in three Cartesian direction and shear forces. The legends are shown in the bottom right of the figures. The range of colours starts with dark blue, it is area of the specimen with no stress. On the other side of the spectrum is red colour. It is the maximum stress in elastic area that is 99 MPa. And the grey colour represent stress the overcome yield stress of the specimen and plasticization occurs.

The first part of this thesis was simulation of static load and relief on axisymmetric semi-space. Figure 16 shows the distribution of Mises stress during the loading process. Grey colored areas are plastic zones. In Figure 16(a) the initial plastic zone occurs in depth that is equal to the perimeter of loading spot. When the maximum load is reached, the plastic zone gets the spherical shape that reaches the depth of the diameter of loading spot. Figure 16(c) shows the zone of residual stress after the stress relief. Residual stress in the surface layer under the loading

spot is close to zero, higher residual stress remains in the depth where the initial plastic area occurred. The secondary plastic zone evolved just next to the area where the load was applied. The secondary plastic zone is related with the shakedown of construction. It can be expressed by shakedown coefficient κ which reads

$$\kappa = \frac{\sigma_{\max}}{\sigma_{\text{pl\_in}}}, \tag{30}$$

where $\sigma_{\max}$ is the maximum stress loaded on the model and $\sigma_{\text{pl\_in}}$ is stress when the first plasticization occurred. In this case, $\sigma_{\max} = 280$ MPa as was said in 3.2. First plastic area appeared when the load was 134 MPa and this state is related with Figure 16(a).

After substitution into the Equation 30

$$\kappa = \frac{280}{134} = 2.09. \tag{31}$$

If $1 < \kappa < 2$, the construction is adapted to the stress. The plasticization arises but residual stresses do not reach yield stress and there is no secondary plasticization. If $\kappa > 2$, residual stresses reach yield stress and the secondary plasticization arises. This is the case of axisymmetric semi-space loaded by pressure of critical value p^{cr} described in Section 3.2.

4.2 Dynamic load

The second simulation using Abaqus/EXPLICIT solver and dynamic load should represent the technology of LSP more exact and the results, mainly shapes of zones of residual stresses, are similar to outcomes of experiments.

Physics of material treatment is shown by the sequence of frames in Figure 17. Frames show evolution of the wave system in the structure after the application of boundary condition that represents the impact of laser. The shown variable is σ_{Mises}. The sequence of pictures shows wave propagation in the material within the time range to 1 μs.

The Figure 17(a) shows the specimen just 0.1 μs after the pulse caused by dynamic force boundary condition that was representing laser pulse during LSP. There is clearly visible the border between loaded and non-loaded area on the surface. The pressure wave is the most powerful. The circle of pressure begins to forming on the mentioned border. This circle is caused by shear forces that arises exactly on this border. The reason is that the pressure forces on the surface right next to non-loaded area in the vertical direction. This ”circle” is actually

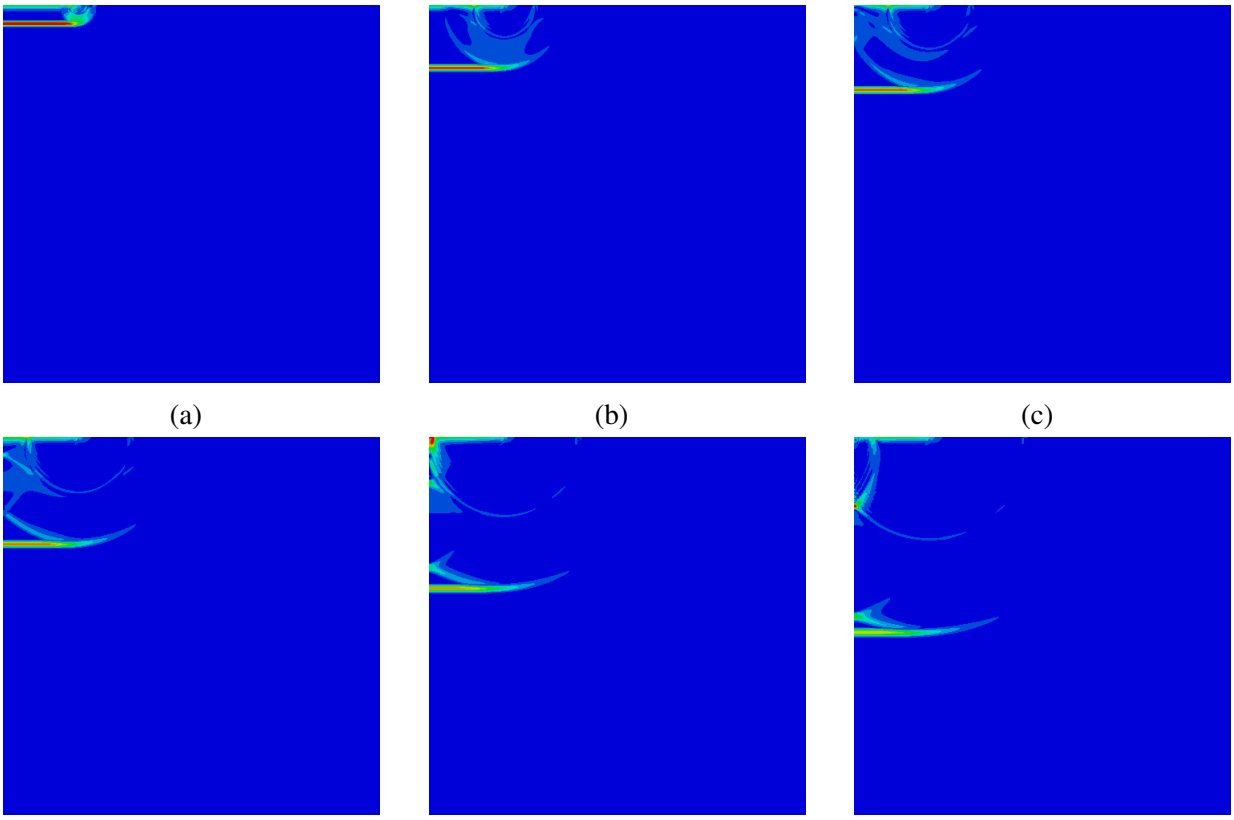

(a) (b) (c)

(d) (e) (f)

Figure 17: Dynamic load

toroid due to axisymmetric geometry and here it will be assigned as shear wave. In detail this wave is shown in Figure 18 where only σ_{12} component is depicted. The time increment is also 0.1μs the same as for Figure 17(a). The figure is also detailed so the middle of it is for $x = 2\text{mm}$.

Already in the first picture are residual stresses in the surface layer. residual stresses indicate the right effect but it is not final stable state. The movement of the primary pressure wave is in three following figures, 17(b),17(c) and 17(d), same as the dissipation of the shear pressure wave. These two waves are still in the contact. Part of the shear wave separates and continues in contact with the primary wave in the Figure 17(d).

The simulation is stopped at time $1\ \mu$s. The wave in this time is depicted in Figure 17(f). It is the time when the wave already lost ability to import residual stresses into the geometry. Keeping the simulation for longer time would bring reflection of the wave from the bottom and subsequent clash with other waves in the system and numerical uncertainty. Thus the simulation is stopped.

The map of residual stress after the static relaxation that was described in Section 3.3 is in

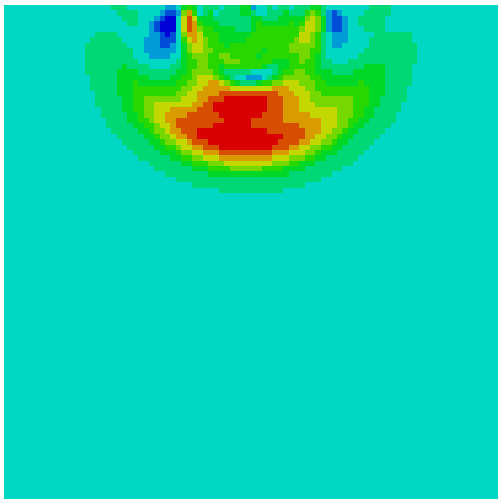

Figure 18: Shear pressure.

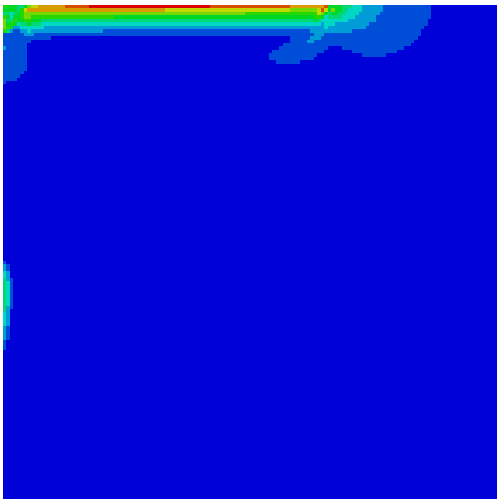

Figure 19: Residual stress.

Figure 19. These results are cleared from all elastic waves that were remaining in explicit simulation. The depicted variable is σ_{Mises} and its shape is similar to expectations based on knowledge from experiments. But the unexpected thing is zone of residual stress in the depth that is equal to perimeter of loading spot.

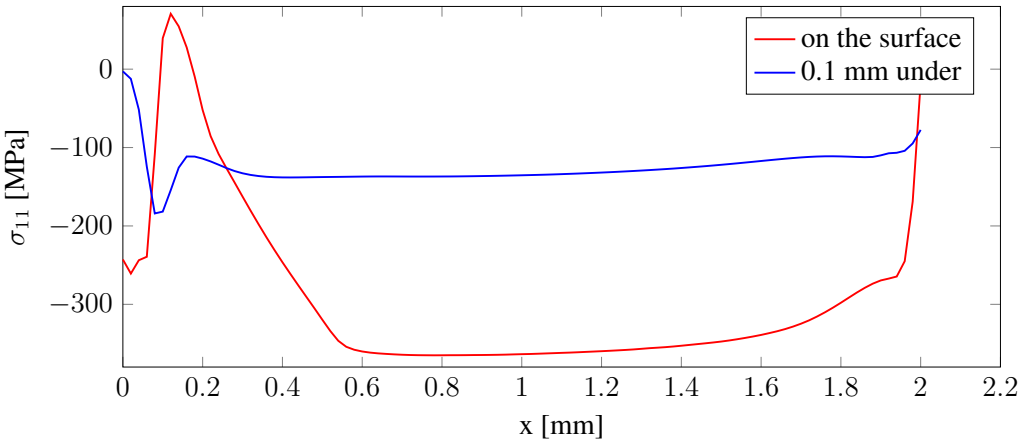

(a)

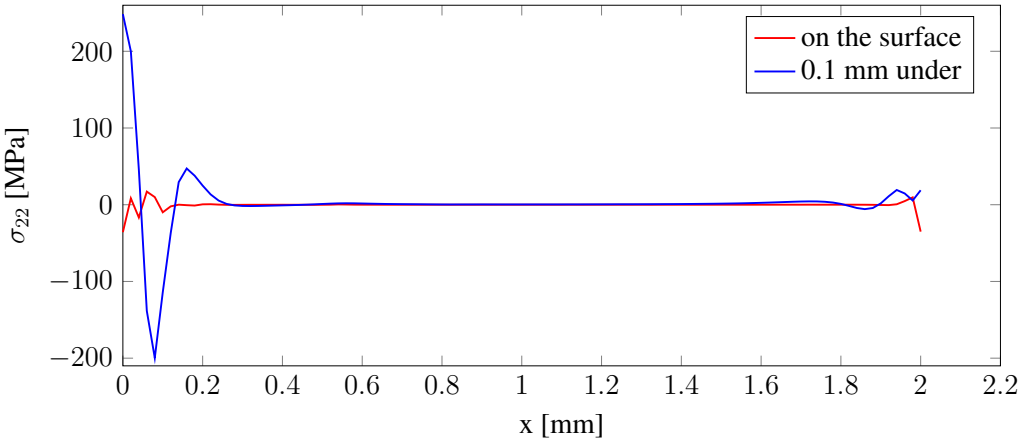

(b)

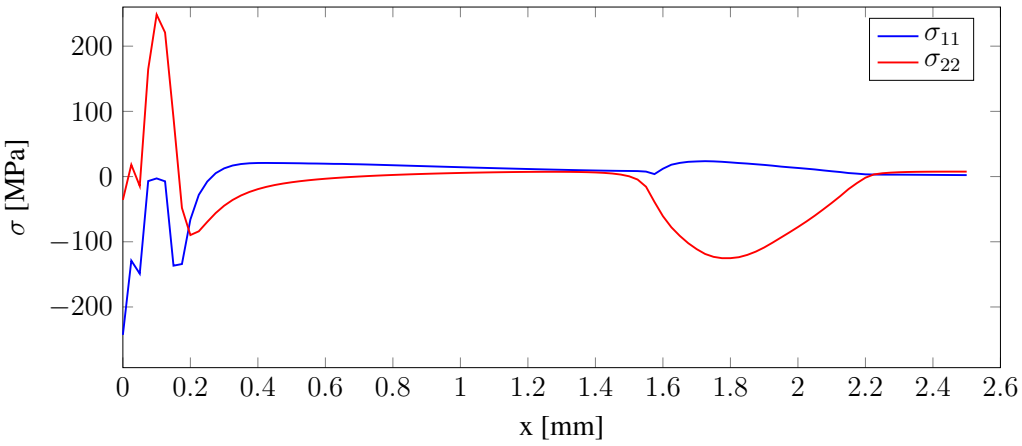

(c)

Figure 20: Course of the residual stresses.

The course of residual stresses is depicted in Figure 20. Figure 20(a) shows component of residual stress σ_{11}, Figure 20(b) shows component of residual stress σ_{22}. Both plots shows the situation in the surface layer what is represented by red curves and in the layer $0.1\,\mathrm{mm}$ under the surface, represented by blue curves. Figure 20(c) shows both components in vertical direction. Plots show ability of LSP to treat the material under the surface and efficiency according to value of reached residual stress. The component that tends to affected the surface layer is σ_{11}. The requirement is to keep values of this component negative. As seen from the plot around the axis of symmetry, σ_{11} turns into positive values, i.e. tensile stresses. This behaviour that simulation shows is in agreement with the experimental observation [6], but this state is opposite to what is desired from LSP. However, the tensile peak is eliminated by the overlap of loading spots during the repetitive application of laser. The shape of the curve and the values are approximately similar to results of FEM simulation of LSP from [5].

In order to verify the simulation, the component σ_{22} on the surface can be checked since its value on the surface is known. It is reaction force against the pressure on the surface. Hence, after the pressure relief, the value of σ_{22} on the surface must be zero. Non-zero values in the plot (Figure 20(b)) comes from the fact that stress values were evaluated not on the surface, but at the integration points.

As seen from Figure 19 and visualized by the curves in Figure 20(c), small area of residual stress occurs in the depth of perimeter of loading spot. This plasticization happens after impact of the shear wave. Magnitude of residual stress is not negligible in the context of numerical simulation. However, its position will not have strong effect on the surface layer, nor the low cycle fatigue properties. Moreover spreading of the shear wave and the wave system in general can be different in material structure due to its imperfection, grains and effect of previous technological treatment.

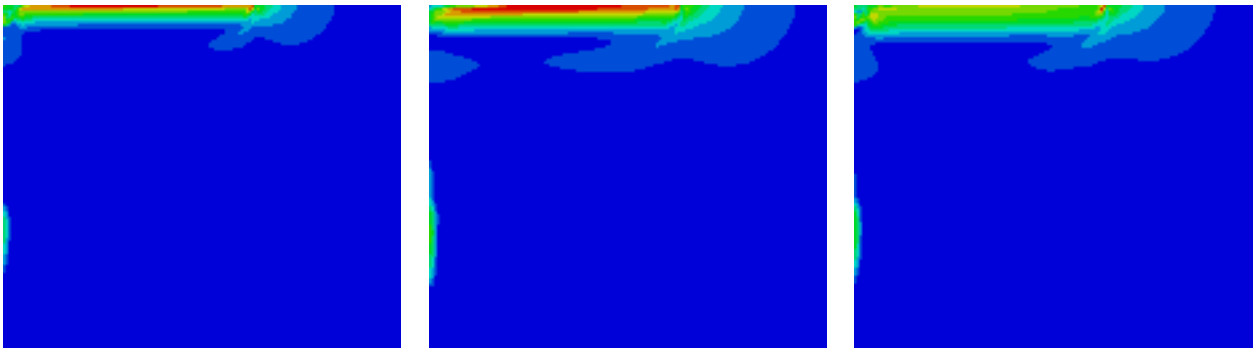

(a) original pulse (b) 30% stronger pulse (c) second pulse coarse

Figure 21: Comparison of pulses.

Two variations of pulse are used in the last part to compare residual stresses for different setting

of pressure. In Figure 21 two different settings of pulse are compared with the original pulse that was estimated in Section 4.2. The first changed parameter was the amplitude of pressure that was settled to $p = 2\,600\ \mathrm{MPa}$. This change caused higher values of residual stress. In the second approach, the shape of pulse with initial amplitude $p = 2\,000\ \mathrm{MPa}$ was changed from the classical tent function to the function that is closer to sinusoidal shape as it is illustrated in Figure 15 by the red line. This change caused deeper zone of residual stress.

5 Conclusions

This thesis was focused on computing of residual stresses in a surface layer due to the use of LSP technology. The methodology was created to simulate LSP in FEM software and output the data of residual stress after the relaxation of material.

The methodology was created on semi-space model with perfect elastic-plastic material model. In the first approach, the process was simulated as a quasi-static problem. These simulations provided knowledge about behaviour of structure with perfect elastic-plastic material and its response to the critical load such as the secondary plasticization. In the second approach, the problem was modeled as waves propagation and their ability to generate residual stresses in a material. Since the LSP process is very fast and its time scale is about 10^{-9} s, very fine spatial step was required, so was the high computational performance. In Section 4, obtained residual stresses are presented. Effect of change of the boundary condition on computed results was studied either.

The static load simulation and the dynamic load simulation can be implemented for different material model by following this thesis. Subsequent work can use this methodology for more complex simulations. The numerical model could be changed from axisymmetric to different geometries. Another proposal for subsequent work is repetition of pulses, study of effect of pulses overlap, etc.

LSP technology that was represented by the dynamic load simulation can be used in hardening process according to computed data. The residual stresses left in the surface after the simulation signified that the treatment was successful and the hardening effect on the surface was done. Only the depth of the residual stresses was smaller than it was expected according to 2.4.4. But as it was mentioned in 4.2, the depth of the affected area can be changed by pulse amplitude, specifically length of the pulse and also its intensity. The resulting magnitude of residual stresses computed in the surface layer correlate with results in [5], so it indicates correctness of computed data. In subsequent work, experimental data would have to be required in order to calibrate parameters of pulse and to validate the simulation.

To sum up the thesis, the FEM simulation of LSP technology helps to understand physical background of this technology. However, many other effects play the role in the quality of treatment and most of them can not be numerically modeled. Thus, numerical modeling gives only a part of the complex knowledge that is necessary to control LSP technology on the level that is sufficient for application in industry.

References

[1] Ankur K. Agrawal and Aparna Singh. *Limitations on the hardness increase in 316L stainless steel under dynamic plastic deformation*. Tech. rep. 2017, pp. 306–312. DOI: https://doi.org/10.1016/j.msea.2017.01.066. URL: https://www.sciencedirect.com/science/article/pii/S0921509317300862.

[2] C. Bathias and A. Pineau. *Fatigue of Materials and Structures*. Tech. rep. 2010.

[3] O. Bilík. *Obrábění II*. Tech. rep. 1994.

[4] L. Börgesson. *ABAQUS*. Tech. rep. 1996, pp. 565–570. DOI: https://doi.org/10.1016/S0165-1250(96)80047-2. URL: https://www.sciencedirect.com/science/article/pii/S0165125096800472.

[5] William Braisted and Robert Brockman. *Finite element simulation of laser shock peening*. Tech. rep. 7. 1999, pp. 719–724. DOI: https://doi.org/10.1016/S0142-1123(99)00035-3. URL: https://www.sciencedirect.com/science/article/pii/S0142112399000353.

[6] J. Brajer. *Vliv metody laser shock processing na integritu povrchu /*. Tech. rep. 2018.

[7] Rudolf Brepta and Miroslav Prokopec. *Šíření napěťových vln a rázy v tělesech*. Czech;English; tech. rep. Praha, 1972.

[8] N. Cristescu. *Dynamic plasticity*. Tech. rep. 2012.

[9] *Deformace materiálu*. Tech. rep. Matematicko-fyzikální fakulta Uninverzity Karlovy, 2020.

[10] G. Dhatt, E. Lefrançois, and G. Touzot. *Finite Element Method*. Tech. rep. 2012. URL: https://books.google.cz/books?id=wvE1ClcHq5IC.

[11] K. Ding. *Three-dimensional Dynamic Finite Element Analysis of Multiple Laser Shock Peening Processes*. Tech. rep. 5. 2003, pp. 351–358. DOI: 10.1179/026708403225007563. eprint: https://doi.org/10.1179/026708403225007563. URL: https://doi.org/10.1179/026708403225007563.

[12] K. Ding and L. Ye. *Laser Shock Peening Performance and Process Simulation*. Tech. rep. 2006.

[13] Anton Du Plessis et al. *Pore Closure Effect of Laser Shock Peening of Additively Manufactured AlSi10Mg*. Oct. 2019. DOI: 10.1089/3dp.2019.0064.

[14] Abdullahi K. Gujba and Mamoun Medraj. *Laser Peening Process and Its Impact on Materials Properties in Comparison with Shot Peening and Ultrasonic Impact Peening*. Tech. rep. 12. 2014, pp. 7925–7974. DOI: 10.3390/ma7127925. URL: https://www.mdpi.com/1996-1944/7/12/7925.

[15] R. Hill. *The Mathematical Theory of Plasticity*. Tech. rep. 1950. URL: https://books.google.cz/books?id=Wy%5C_kuQZzfdIC.

[16] C. Höschl. *Únava materiálu při periodickém zatěžování*. Tech. rep. 1981.

[17] I Jeník. *Identifikace parametrů elasto-plastických modelů materiálu z experimentálních dat*. Tech. rep. 2015.

[18] A. S. Kaygorodov and S. V. Zayats. *Dynamic plastic deformation of metal-matrix composites*. English. Tech. rep. 2. Sept. 2020. URL: https://www.proquest.com/scholarly-journals/dynamic-plastic-deformation-metal-matrix/docview/2562755515/se-2.

[19] A.S. Khan and S. Huang. *Continuum Theory of Plasticity*. Tech. rep. 1995. URL: https://books.google.cz/books?id=l1FPaaY355gC.

[20] Cheol-Ho Lee. *Structural Performance of 800 MPa High-Strength Steel Members and Application to Highrise and Mega Building Structures*. Tech. rep. 3. 2017, pp. 249–259.

[21] Hongjun Li, Jian Gao, and Qinchuan Li. *Fatigue of Friction Stir Welded Aluminum Alloy Joints: A Review*. Tech. rep. 12. 2018. DOI: 10.3390/app8122626. URL: https://www.mdpi.com/2076-3417/8/12/2626.

[22] J. Lubliner. *Plasticity Theory*. Tech. rep. 2008. URL: https://books.google.cz/books?id=MkK-BLbHtcAC.

[23] H. Matsuoka and T. Nakai. *RELATIONSHIP AMONG TRESCA, MISES, MOHR-COULOMB AND MATSUOKA-NAKAI FAILURE CRITERIA*. Tech. rep. 4. 1985, pp. 123–128. DOI: 10.3208/sandf1972.25.4_123.

[24] Xiao-Long Nan et al. *Effect of c/a axial ratio on Schmid factors in hexagonal close-packed metals*. Tech. rep. 7. 2013, pp. 530–533. DOI: https://doi.org/10.1016/j.scriptamat.2012.12.006. URL: https://www.sciencedirect.com/science/article/pii/S1359646212007774.

[25] Yasuo Ochi et al. *Effect of shot-peening treatment on high cycle fatigue property of ductile cast iron*. Tech. rep. 5. 2001, pp. 441–448. DOI: https://doi.org/10.1016/S0142-1123(00)00110-9. URL: https://www.sciencedirect.com/science/article/pii/S0142112300001109.

[26] M. Piao et al. *Characterization of flow stress at ultra-high strain rates by proper extrapolation with Taylor impact tests*. Tech. rep. 2016, pp. 142–157. DOI: https://doi.org/10.1016/j.ijimpeng.2016.01.004. URL: https://www.sciencedirect.com/science/article/pii/S0734743X16300094.

[27] MingJun Piao et al. *Characterization of hardening behaviors of 4130 Steel, OFHC Copper, Ti6Al4V alloy considering ultra-high strain rates and high temperatures*. Tech. rep. 2017, pp. 1117–1129. DOI: https://doi.org/10.1016/j.ijmecsci.2017.08.013. URL: https://www.sciencedirect.com/science/article/pii/S0020740316307378.

[28] *Plasticity theory for fibre-reinforced composites*. Tech. rep. 1992, p. 118. DOI: 10.1007/BF00043230. URL: https://doi.org/10.1007/BF00043230.

[29] J. Polák. *Cyklická plasticita a nízkocyklová únavová odolnost kovových materiálů /*. Tech. rep. 1991, p. 314.

[30] Udomsak Rotpai et al. *Novel flow stress prediction and work hardening behavior of aluminium alloy AA7075 at room and elevated temperatures*. Tech. rep. 2022, p. 162013. DOI: https://doi.org/10.1016/j.jallcom.2021.162013. URL: https://www.sciencedirect.com/science/article/pii/S0925838821034228.

[31] M. Růžička M. Hanke and M. Rost. *Dynamická pevnost a životnost*. Tech. rep. 1987.

[32] Aviral Shrot and Martin Bäker. *Determination of Johnson–Cook parameters from machining simulations*. Tech. rep. 1. Proceedings of the 20th International Workshop on Computational Mechanics of Materials - IWCMM 20. 2012, pp. 298–304. DOI: https://doi.org/10.1016/j.commatsci.2011.07.035. URL: https://www.sciencedirect.com/science/article/pii/S0927025611004277.

[33] F. Tschuchnigg, H.F. Schweiger, and S.W. Sloan. *Slope stability analysis by means of finite element limit analysis and finite element strength reduction techniques. Part II: Back analyses of a case history*. Tech. rep. 2015, pp. 178–189. DOI: https://doi.org/10.1016/j.compgeo.2015.07.019. URL: https://www.sciencedirect.com/science/article/pii/S0266352X15001767.

[34] Wang and C. James. *Young´s modulus of porous materials*. Tech. rep. 1984. DOI: 10.1007/BF00540451. URL: https://doi.org/10.1007/BF00540451.